Exact Coherent States: Variational Methods

Rich Kerswell

Lectures 5 & 6

DRAFT May 21, 2019

1 Transient Dynamics: Non-Modal Analysis

Linear stability analysis does not necessarily give the whole picture of what the dynamics can be in the neighbourhood of a state. If the linear operator L is non-normal, i.e.

$$L^+L \neq LL^+ \tag{1}$$

(where L^+ is the adjoint operator and so this property depends on the inner product being used), then growth in the norm (e.g. kinetic energy) associated with the inner product (e.g. the energy inner product) can occur despite L only having decaying eigenvalues. Let's look at a simple matrix example

$$\frac{d}{dt}\begin{bmatrix} x_1 \\ x_2 \end{bmatrix} = L\begin{bmatrix} x_1 \\ x_2 \end{bmatrix} := \begin{bmatrix} \lambda_1 & 1 \\ 0 & \lambda_2 \end{bmatrix}\begin{bmatrix} x_1 \\ x_2 \end{bmatrix} \tag{2}$$

where $\lambda_1, \lambda_2 < 0$ (assume real and negative for simplicity although the key thing is that their real parts are negative). This L has eigenvalues λ_1 and λ_2 and so a linear analysis (around the state $\mathbf{x} = \mathbf{0}$) predicts exponential decay for all small disturbances. However this is only true in a long time sense. Consider the energy inner product,

$$E(t) := \mathbf{x}(t)^T \cdot \mathbf{x}(t) = x_1^2(t) + x_2^2(t), \tag{3}$$

then

$$\frac{dE}{dt} = 2\mathbf{x}^T \begin{bmatrix} \lambda_1 & \frac{1}{2} \\ \frac{1}{2} & \lambda_2 \end{bmatrix}\mathbf{x}. \tag{4}$$

The eigenvalues of this symmetric matrix are

$$\tfrac{1}{2}(\lambda_1 + \lambda_2) \pm \tfrac{1}{2}\sqrt{(\lambda_1 - \lambda_2)^2 + 1} \tag{5}$$

so there can be energy growth if

$$\sqrt{(\lambda_1-\lambda_2)^2+1} > -(\lambda_1+\lambda_2) > 0 \tag{6}$$

which can easily be arranged (e.g. $\lambda_1, \lambda_2 \ll 1$). The point is that L is a non-normal matrix and so its eigenvectors

$$\mathbf{e}_1 := \begin{bmatrix} 1 \\ 0 \end{bmatrix} \quad \& \quad \mathbf{e}_2 := \begin{bmatrix} 1 \\ (\lambda_2-\lambda_1) \end{bmatrix} \tag{7}$$

are not orthogonal[1]: in fact $\mathbf{e}_2^T \cdot \mathbf{e}_1 = 1$ which is the same size as $\mathbf{e}_1^T \cdot \mathbf{e}_1$ and $\mathbf{e}_2^T \cdot \mathbf{e}_2$. This means in general that there are initial conditions which are 'inefficiently' represented. For example, the initial condition

$$\mathbf{x}(0) = \begin{bmatrix} 0 \\ 1 \end{bmatrix} = \frac{1}{\lambda_2-\lambda_1}\left(\mathbf{e}_2 - \mathbf{e}_1\right), \tag{8}$$

gives rise to the solution

$$\mathbf{x}(t) = \frac{1}{\lambda_2-\lambda_1}\left(\mathbf{e}_2 e^{\lambda_2 t} - \mathbf{e}_1 e^{\lambda_1 t}\right), \tag{9}$$

which, over a timescale $O([\max(-\lambda_1,-\lambda_2)]^{-1})$, will grow from $O(1)$ energy to $O(\lambda_2-\lambda_1)^{-2})$ as the initial cancellation no longer occurs.

Calculating the largest possible energy growth

$$G(T) := \max_{\mathbf{x}(0)} \frac{E(T)}{E(0)} \tag{10}$$

some time T later is a more useful way of quantifying the phenomenon. The solution of (2) is

$$\mathbf{x}(t) = e^{Lt}\mathbf{x}(0) = \begin{bmatrix} e^{\lambda_1 t} & \frac{e^{\lambda_1 t}-e^{\lambda_2 t}}{\lambda_1-\lambda_2} \\ 0 & e^{\lambda_2 t} \end{bmatrix} \mathbf{x}(0), \tag{11}$$

(show by induction that

$$L^n := \begin{bmatrix} \lambda_1^n & \frac{\lambda_1^n-\lambda_2^n}{\lambda_1-\lambda_2} \\ 0 & \lambda_2^n \end{bmatrix} \quad \& \quad \text{use} \quad e^{Lt} = \sum_{n=0} \frac{(Lt)^n}{n!} \quad),$$

so

$$G(T) := \max_{\mathbf{x}(0)} \frac{\mathbf{x}(0)^T \mathbb{A}(T) \mathbf{x}(0)}{\mathbf{x}(0)^T \mathbf{x}(0)} \tag{12}$$

where

$$\mathbb{A}(T) := e^{L^+T} e^{LT} = \begin{bmatrix} e^{2\lambda_1 T} & e^{\lambda_1 T}\left(\frac{e^{\lambda_1 T}-e^{\lambda_2 T}}{\lambda_1-\lambda_2}\right) \\ e^{\lambda_1 T}\left(\frac{e^{\lambda_1 T}-e^{\lambda_2 T}}{\lambda_1-\lambda_2}\right) & e^{2\lambda_2 T} + \left(\frac{e^{\lambda_1 T}-e^{\lambda_2 T}}{\lambda_1-\lambda_2}\right)^2 \end{bmatrix}. \tag{13}$$

Since $\mathbb{A}$ is real and symmetric (and coincidentally positive definite since $G > 0$), the process of maximization is done simply by identifying the largest (real) eigenvalue of $\mathbb{A}$ and the optimal initial condition $\mathbf{x}(0)$ is then simply the corresponding eigenvector.

[1] A normal matrix $\Leftrightarrow \exists$ a complete set of orthogonal eigenvectors.

1.1 Matrix-based Approach

Returning to the Navier-Stokes equations, we can linearize around some solution $\mathbf{U}$ so that

$$\frac{\partial \mathbf{u}}{\partial t} = L\mathbf{u}, \tag{14}$$

where L is a linear operator, which has eigenvalues λ_j and eigenfunctions $\mathbf{q}_j$. Assuming that the set $\mathbf{q}_j$ is complete (but not necessarily orthogonal unless L is normal), then

$$\mathbf{u}_0(\mathbf{x}) = \sum_{j=1}^{\infty} a_j(0)\mathbf{q}_j(\mathbf{x}) \quad \Rightarrow \quad \mathbf{u}(\mathbf{x},t) = \sum_{j=1}^{\infty} a_j(t)\mathbf{q}_j(\mathbf{x}) \tag{15}$$

where $a_j(t) := a_j(0)\exp(\lambda_j t)$. Then

$$G(T;Re) = \max_{\mathbf{a(0)}} \frac{\langle\, \mathbf{u}^* \,.\, \mathbf{u} \,\rangle}{\langle\, \mathbf{u}_0^* \,.\, \mathbf{u}_0 \,\rangle} = \max_{\mathbf{a(0)}} \frac{\sum_i \sum_j a_i^*(T)a_j(T)\langle\, \mathbf{q}_i^* . \mathbf{q}_j \,\rangle}{\sum_i \sum_j a_i^*(0)a_j(0)\langle\, \mathbf{q}_i^* . \mathbf{q}_j \,\rangle}. \tag{16}$$

Truncating at some large but finite N (so things become finite-dimensional yet insensitive to the exact value of N) then $M_{ij} := \langle\, \mathbf{q}_i^* . \mathbf{q}_j \,\rangle$ is a Hermitian $n \times n$ matrix which can be reduced to another matrix F such that $F^*F = M$, then

$$G(T;Re) = \max_{\mathbf{a(0)}} \frac{[F\mathbf{a}(T)]^* . F\mathbf{a}(T)}{[F\mathbf{a}(0)]^* . F\mathbf{a}(0)} = \max_{\mathbf{a(0)}} \frac{[Fe^{\Lambda T}\mathbf{a}(0)]^* . Fe^{\Lambda T}\mathbf{a}(0)}{[F\mathbf{a}(0)]^* . F\mathbf{a}(0)} = ||Fe^{\Lambda T}F^{-1}||_2^2 \tag{17}$$

where $e^{\Lambda T} = \mathrm{diag}(e^{\lambda_1 T}, e^{\lambda_2 T}, \ldots, e^{\lambda_N T})$ [17]. This can handled by standard Singular Value Decomposition (SVD) software to give the largest singular value. If L is normal, M and F are diagonal and

$$G(T;Re) = ||e^{\Lambda T}||_2^2 = \max_j \left|e^{\lambda_j T}\right|^2 = \max_j e^{2\Re e(\lambda_j)T} \tag{18}$$

so there can be no transient growth when L is linearly stable i.e. $\Re e(\lambda_j) \leq 0$ for all j.

This method is straightforward but only really computationally feasible for one-dimensional, or possibly two-dimensional problems because the size of the matrices becomes unwieldy and then unmanageable for three-dimensional problems. A better approach is the matrix-free method which, although incurring more start-up costs (e.g. building a time stepping algorithm), is extendable to include nonlinearity.

1.2 Matrix-free Method

We now consider the use of a matrix-free variational method for finding the energy growth which involves time-stepping the linearised Navier-Stokes equations. Since

the problem is linear, the initial energy can be rescaled to 1 and we consider the Lagrangian

$$G = G(\mathbf{u}, p, \lambda, \boldsymbol{\nu}, \pi; T) = \left\langle \frac{1}{2}|\mathbf{u}(\mathbf{x}, T)|^2 \right\rangle + \lambda \left\{ \left\langle \frac{1}{2}|\mathbf{u}(\mathbf{x}, 0)|^2 \right\rangle - 1 \right\}$$
$$+ \int_0^T \left\langle \boldsymbol{\nu}(\mathbf{x}, t) \cdot \left\{ \frac{\partial \mathbf{u}}{\partial t} + (\mathbf{u}_{\text{lam}} \cdot \nabla)\mathbf{u} + (\mathbf{u} \cdot \nabla)\mathbf{u}_{\text{lam}} + \nabla p - \frac{1}{Re}\nabla^2 \mathbf{u} \right\} \right\rangle dt$$
$$+ \int_0^T \langle \pi(\mathbf{x}, t) \nabla \cdot \mathbf{u} \rangle \, dt \tag{19}$$

where λ, $\boldsymbol{\nu}$ and π are Lagrangian multipliers imposing the constraints that the initial energy is fixed, that the linearized Navier-Stokes equation holds over $t \in [0, T]$ and the flow is incompressible (their corresponding Euler-Lagrange equations are respectively:

$$\left\langle \frac{1}{2}|\mathbf{u}(\mathbf{x}, 0)|^2 \right\rangle = 1, \tag{20}$$
$$\frac{\partial \mathbf{u}}{\partial t} + (\mathbf{u}_{\text{lam}} \cdot \nabla)\mathbf{u} + (\mathbf{u} \cdot \nabla)\mathbf{u}_{\text{lam}} + \nabla p - \frac{1}{Re}\nabla^2 \mathbf{u} = 0, \tag{21}$$
$$\nabla \cdot \mathbf{u} = 0.) \tag{22}$$

The Euler-Lagrange equation for the pressure p is

$$0 = \int_0^T \left\langle \frac{\delta G}{\delta p} \delta p \right\rangle dt = \int_0^T \langle (\boldsymbol{\nu} \cdot \nabla)\delta p \rangle \, dt$$
$$= \int_0^T \langle \nabla \cdot (\boldsymbol{\nu} \delta p) \rangle \, dt - \int_0^T \langle \delta p (\nabla \cdot \boldsymbol{\nu}) \rangle \, dt. \tag{23}$$

which to vanish means

$$\boldsymbol{\nu} = \mathbf{0} \ \text{ at boundary}, \tag{24}$$
$$\nabla \cdot \boldsymbol{\nu} = 0. \tag{25}$$

Now, considering variations in $\mathbf{u}$ (with the condition that $\delta \mathbf{u} = \mathbf{0}$ on the boundary):

$$\int_0^T \left\langle \frac{\delta G}{\delta \mathbf{u}} \cdot \delta \mathbf{u} \right\rangle = \langle \mathbf{u}(\mathbf{x}, T) \cdot \delta \mathbf{u}(\mathbf{x}, T) \rangle + \lambda \langle \mathbf{u}(\mathbf{x}, 0) \cdot \delta \mathbf{u}(\mathbf{x}, 0) \rangle$$
$$+ \int_0^T \left\langle \boldsymbol{\nu} \cdot \left\{ \frac{\partial \delta \mathbf{u}}{\partial t} + (\mathbf{u}_{\text{lam}} \cdot \nabla)\delta \mathbf{u} + (\delta \mathbf{u} \cdot \nabla)\mathbf{u}_{\text{lam}} - \frac{1}{Re}\nabla^2 \delta \mathbf{u} \right\} \right\rangle dt$$
$$+ \int_0^T \langle \pi \nabla \cdot \delta \mathbf{u} \rangle \, dt. \tag{26}$$

The first term in the second line of the above equation can be reexpressed as

$$\int_0^T \left\langle \boldsymbol{\nu} \cdot \frac{\partial \delta \mathbf{u}}{\partial t} \right\rangle dt = \int_0^T \left\langle \frac{\partial}{\partial t}(\delta \mathbf{u} \cdot \boldsymbol{\nu}) \right\rangle dt - \int_0^T \left\langle \delta \mathbf{u} \cdot \frac{\partial \boldsymbol{\nu}}{\partial t} \right\rangle dt$$
$$= \langle \delta \mathbf{u}(\mathbf{x}, T) \cdot \boldsymbol{\nu}(\mathbf{x}, T) - \delta \mathbf{u}(\mathbf{x}, 0) \cdot \boldsymbol{\nu}(\mathbf{x}, 0) \rangle - \int_0^T \left\langle \delta \mathbf{u} \cdot \frac{\partial \boldsymbol{\nu}}{\partial t} \right\rangle dt, \tag{27}$$

the second term as

$$\langle \boldsymbol{\nu} \cdot \{(\mathbf{u}_{\text{lam}} \cdot \nabla) \delta \mathbf{u}\} \rangle = \langle \nabla \cdot ((\boldsymbol{\nu} \cdot \delta \mathbf{u}) \mathbf{u}_{\text{lam}}) - \delta \mathbf{u} \cdot \{(\mathbf{u}_{\text{lam}} \cdot \nabla) \boldsymbol{\nu}\} \rangle$$
$$= - \langle \delta \mathbf{u} \cdot \{(\mathbf{u}_{\text{lam}} \cdot \nabla) \boldsymbol{\nu}\} \rangle , \tag{28}$$

the third term as

$$\langle \boldsymbol{\nu} \cdot \{(\delta \mathbf{u} \cdot \nabla) \mathbf{u}_{\text{lam}}\} \rangle = \left\langle \delta \mathbf{u} \cdot \left\{ \boldsymbol{\nu} \cdot (\nabla \mathbf{u}_{\text{lam}})^{\mathrm{T}} \right\} \right\rangle (= \langle \delta u_i \ \nu_j \ \partial_i u_{\text{lam},j} \rangle). \tag{29}$$

and the fourth term as

$$\left\langle \boldsymbol{\nu} \cdot \left(-\frac{1}{Re} \nabla^2 \delta \mathbf{u} \right) \right\rangle = - \left\langle \frac{1}{Re} \delta \mathbf{u} \cdot \nabla^2 \boldsymbol{\nu} \right\rangle , \tag{30}$$

and finally the last term as

$$\langle \pi \nabla \cdot \delta \mathbf{u} \rangle = \langle \nabla \cdot \pi \delta \mathbf{u} \rangle - \langle \delta \mathbf{u} \cdot \nabla \pi \rangle$$
$$= - \langle \delta \mathbf{u} \cdot \nabla \pi \rangle . \tag{31}$$

Combining all these gives

$$\int_0^T \left\langle \frac{\delta G}{\delta \mathbf{u}} \cdot \delta \mathbf{u} \right\rangle = \langle \delta \mathbf{u}(\mathbf{x}, T) \cdot \{\mathbf{u}(\mathbf{x}, T) + \boldsymbol{\nu}(\mathbf{x}, T)\} \rangle + \langle \delta \mathbf{u}(\mathbf{x}, 0) \cdot \{\lambda \mathbf{u}(\mathbf{x}, 0) - \boldsymbol{\nu}(\mathbf{x}, 0)\} \rangle$$
$$+ \int_0^T \left\langle \delta \mathbf{u} \cdot \left\{ -\frac{\partial \boldsymbol{\nu}}{\partial t} - (\mathbf{u}_{\text{lam}} \cdot \nabla) \boldsymbol{\nu} + \boldsymbol{\nu} \cdot (\nabla \mathbf{u}_{\text{lam}})^{\mathrm{T}} - \nabla \pi - \frac{1}{Re} \nabla^2 \boldsymbol{\nu} \right\} \right\rangle dt. \tag{32}$$

For this to vanish for all allowed $\delta \mathbf{u}(\mathbf{x}, T)$, $\delta \mathbf{u}(\mathbf{x}, 0)$ and $\delta \mathbf{u}$ means

$$\frac{\delta G}{\delta \mathbf{u}(\mathbf{x}, T)} = 0 \quad \Rightarrow \quad \mathbf{u}(\mathbf{x}, T) + \boldsymbol{\nu}(\mathbf{x}, T) = \mathbf{0} \tag{33}$$

$$\frac{\delta G}{\delta \mathbf{u}(\mathbf{x}, 0)} = 0 \quad \Rightarrow \quad \lambda \mathbf{u}(\mathbf{x}, 0) - \boldsymbol{\nu}(\mathbf{x}, 0) = \mathbf{0} \tag{34}$$

$$\frac{\delta G}{\delta \mathbf{u}} = 0 \quad \Rightarrow \quad \frac{\partial \boldsymbol{\nu}}{\partial t} + (\mathbf{u}_{\text{lam}} \cdot \nabla) \boldsymbol{\nu} - \boldsymbol{\nu} \cdot (\nabla \mathbf{u}_{\text{lam}})^{\mathrm{T}} + \nabla \pi + \frac{1}{Re} \nabla^2 \boldsymbol{\nu} = \mathbf{0}. \tag{35}$$

The last equation is the 'dual (or adjoint) linearized Navier-Stokes equation'. This equation can only be integrated backwards in time because of the negative diffusion term. Figure 1 shows a diagram of a numerical method for iteratively solving these variational equations in order to construct the initial condition with maximum growth (e.g. [5]). The algorithm has the following steps.

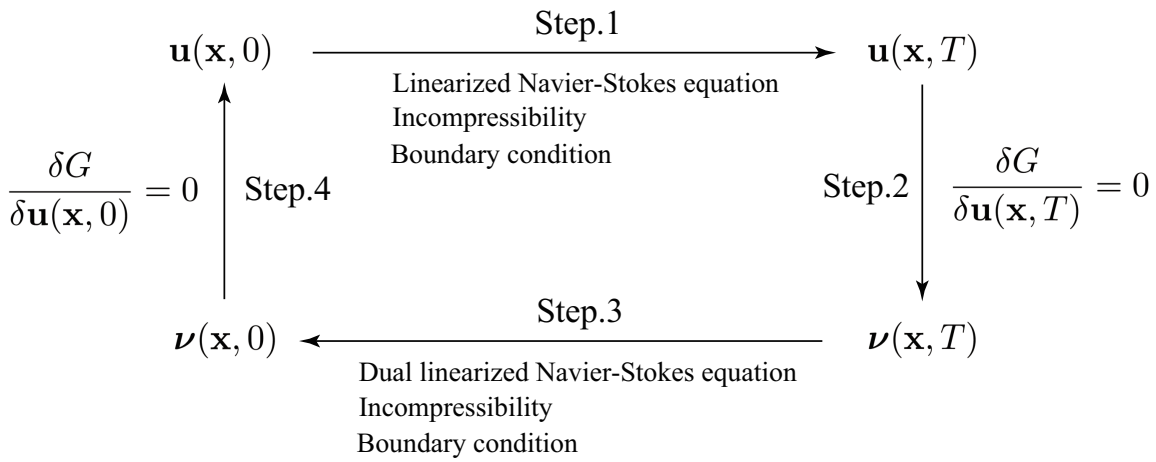

Figure 1: Diagram of iterative method.

Step.0 Choose an initial condition of the iterative method $\mathbf{u}^{(0)}(\mathbf{x},0)$ such that

$$\left\langle \frac{1}{2}\left\{\mathbf{u}^{(0)}(\mathbf{x},0)\right\}^2 \right\rangle = 1. \tag{36}$$

Then we construct $\mathbf{u}^{(n+1)}(\mathbf{x},0)$ from $\mathbf{u}^{(n)}(\mathbf{x},0)$ as follows:

Step.1 Time integrate the linearized Navier-Stokes equation forward with incompressibility $\nabla \cdot \mathbf{u} = 0$ and boundary condition $\mathbf{u} = \mathbf{0}$ from $t = 0$ to $t = T$ with the initial condition $\mathbf{u}^{(n)}(\mathbf{x},0)$ to find $\mathbf{u}^{(n)}(\mathbf{x},T)$.

Step.2 Calculate $\boldsymbol{\nu}^{(n)}(\mathbf{x},T)$ using (33) which is then used as the *initial* condition for the dual linearized Navier-Stokes equation (35).

Step.3 Backwards time integrate the dual linearized Navier-Stokes equation (35) with incompressibility (25) and boundary condition (24) from $t = T$ to $t = 0$ with the 'initial' condition $\boldsymbol{\nu}^{(n)}(\mathbf{x},T)$ to find $\boldsymbol{\nu}^{(n)}(\mathbf{x},0)$.

Step.4 Using equation (34), a simple approach to calculating the correction of $\mathbf{u}^{(n)}$ is as follows:

$$\mathbf{u}^{(n+1)} = \mathbf{u}^{(n)} + \epsilon \left[\frac{\delta G}{\delta \mathbf{u}(\mathbf{x},0)}\right]^{(n)} \tag{37}$$

$$= \mathbf{u}^{(n)} + \epsilon \left(\lambda \mathbf{u}^{(n)}(\mathbf{x},0) - \boldsymbol{\nu}^{(n)}(\mathbf{x},0)\right), \tag{38}$$

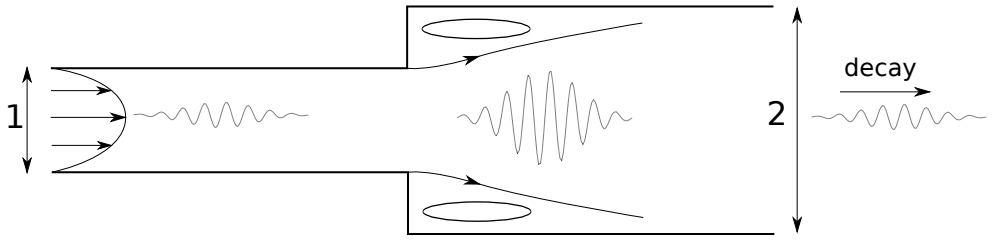

Figure 2: Initial noise is magnified as it passes through the pipe expansion before eventually decaying.

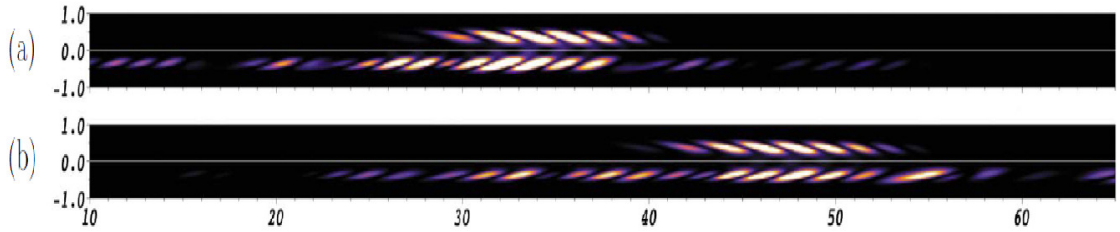

Figure 3: Comparison between noise-driven flows (bottom halves) and the linear optimal growth (top halves) for $Re = 900$ (upper) and $Re = 1200$ (lower) [1].

with λ chosen such that

$$1 = \left\langle \frac{1}{2} \left\{ \mathbf{u}^{(n+1)}(\mathbf{x}, 0) \right\}^2 \right\rangle \tag{39}$$

$$= \left\langle \frac{1}{2} \left[(1 + \epsilon\lambda)\mathbf{u}^{(n)}(\mathbf{x}, 0) - \epsilon \boldsymbol{\nu}^{(n)}(\mathbf{x}, 0) \right]^2 \right\rangle . \tag{40}$$

Here ϵ is a parameter of this iterative method and must be sufficiently small.

This last step moves $\mathbf{u}^{(n)}(\mathbf{x}, 0)$ in the direction of maximum ascent in order to increase $G(T)$. Iterating the last four steps typically converges to a local maximum of $G(T)$ [3], [5].

An example of the application of this method for finding linear optimum initial conditions is the case of expansion flow in a pipe [1], see Figure 2. Flow through an expansion in a pipe is a classical engineering problem which is not spatially homogeneous. The resulting linear-growth optimal can be compared with the numerical result of perturbing the flow with random noise, see Figure 3. The dominant spatial structure which grows out of the noise appears to agree well with the linear optimal.

1.3 Nonlinear Extension

The matrix-free approach is, in principle, 'easily' extended to the non-linear problem. There are only two changes that need to be made to the Lagrangian G: the nonlinearity is added back to the linearised Navier-Stokes equation and the initial energy is explicitly set at E_0 which joins T as a free parameter of the problem. So

$$G(T, E_0; Re) = ... + \int_0^T \langle \boldsymbol{\nu} \cdot (\mathbf{u} \cdot \nabla)\mathbf{u} \rangle \, dt + \lambda \left\{ \left\langle \frac{1}{2}\mathbf{u}^2(x, 0) \right\rangle - E_0 \right\} \tag{41}$$

(notice now that G/E_0 is the energy growth factor but it's simpler to just do this division after the optimization). The addition of the non-linear term means that the part of the functional derivative of G with respect to $\mathbf{u}$ must be recalculated to get

$$\begin{aligned} \int_0^T \left\langle \frac{\delta G}{\delta \mathbf{u}} \cdot \delta\mathbf{u} \right\rangle dt &= ... + \int_0^T \langle \boldsymbol{\nu} \cdot [\delta\mathbf{u} \cdot \nabla\mathbf{u} + \mathbf{u} \cdot \nabla\delta\mathbf{u}] \rangle \, dt \\ &= ... + \int_0^T \left\langle \delta\mathbf{u} \cdot [(\nabla\mathbf{u})^{\mathrm{T}} \cdot \boldsymbol{\nu} - \mathbf{u} \cdot \nabla\boldsymbol{\nu}] \right\rangle dt. \end{aligned} \tag{42}$$

Then the dual Navier-Stokes equation becomes

$$-\frac{\partial \boldsymbol{\nu}}{\partial t} + (\nabla[\mathbf{u} + \mathbf{u}_{lam}])^{\mathrm{T}} \cdot \boldsymbol{\nu} - (\mathbf{u} + \mathbf{u}_{lam}) \cdot \nabla\boldsymbol{\nu} - \nabla\pi - \frac{1}{Re}\nabla^2\boldsymbol{\nu} = 0. \tag{43}$$

The consequences of adding the non-linear term can be summarised as follows:

1. The full Navier-Stokes equations now need to be integrated forward in time.
2. The dual Navier-Stokes equation remains linear in $\boldsymbol{\nu}$ but now depends on $\mathbf{u}(\mathbf{x}, t)$.
3. The result depends on *both* E_0 and T.

The added dependence of the dual equations on $\mathbf{u}(\mathbf{x}, t)$ creates some problems numerically as this suggests that $\mathbf{u}(\mathbf{x}, t)$ must be stored at every step of the forwards integration. For large systems the memory requirements associated with this are unfeasible so a method called 'checkpointing' is used instead. This involves storing $\mathbf{u}(\mathbf{x}, t)$ at a reduced set of times or 'checkpoints' and then integrating forward in time again from each checkpoint as required when calculating $\boldsymbol{\nu}$, see figure 4. This method results in much reduced storage requirements but at the added cost of having to perform the forward integration twice per iteration.

1.4 Minimal Seed Analysis

The simple idea is to examine $G(T = \text{'}\infty\text{'}, E_0)$ as a function of E_0 with the objective of detecting a sudden jump in the value of G corresponding to initial conditions

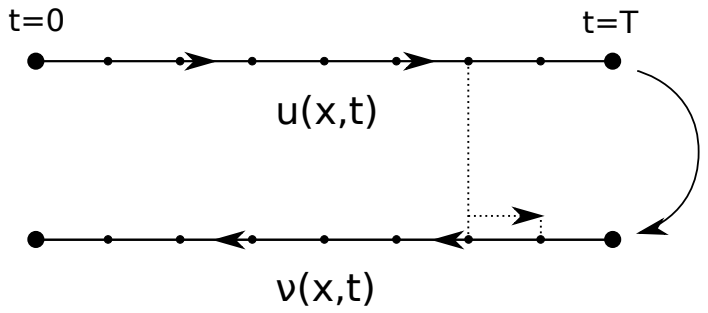

Figure 4: Checkpointing: during the calculation of $\boldsymbol{\nu}(\mathbf{x},t)$ the velocity $\mathbf{u}(\mathbf{x},t)$ is recalculated in short sections from each checkpoint.

suddenly having access to a different basin of attraction. To illustrate this, let's go back to our trusty 2 ODE model

$$\begin{aligned} \dot{x_1} &= f_1(x_1,x_2) := -x_1 + 10x_2, \\ \dot{x_2} &= f_2(x_1,x_2) := x_2(10\mathrm{e}^{-0.01x_1^2} - x_2)\,(x_2-1)\,, \end{aligned} \tag{44}$$

and define

$$\mathcal{L} := \mathbf{x}^2(T) - \lambda[E_0 - \mathbf{x}^2(0)] + \int_0^T \boldsymbol{\nu}(t)\cdot\left[\frac{d\mathbf{x}}{dt} - \mathbf{f}(\mathbf{x})\right]\,dt \tag{45}$$

where $\mathbf{f}(\mathbf{x}) = (f_1, f_2)$ is the right hand side in (44). The Euler-Lagrange equations for stationarizing $\mathcal{L}$ are

$$\frac{\delta\mathcal{L}}{\delta\boldsymbol{\nu}} := \frac{d\mathbf{x}}{dt} - \begin{bmatrix} -x_1 + 10x_2 \\ x_2(10e^{-x_1^2/100} - x_2)(x_2-1) \end{bmatrix} = \mathbf{0}, \tag{46}$$

$$\frac{\delta\mathcal{L}}{\delta\mathbf{x}} := -\frac{d\boldsymbol{\nu}}{dt} + \begin{bmatrix} \nu_1 + \frac{1}{5}x_1\nu_2(x_2^2 - x_2)e^{-x_1^2/100} \\ -10\nu_1 + \nu_2(3x_2^2 - 2x_2) - 10\nu_2(2x_2-1)e^{-x_1^2/100} \end{bmatrix} = \mathbf{0}, \tag{47}$$

$$\frac{\delta\mathcal{L}}{\delta\mathbf{x}(0)} := 2\lambda\mathbf{x}(0) - \boldsymbol{\nu}(0) = 0, \tag{48}$$

$$\frac{\delta\mathcal{L}}{\delta\mathbf{x}(T)} := 2\mathbf{x}(T) + \boldsymbol{\nu}(T) = 0, \tag{49}$$

The solution strategy is to start with a guess for the initial condition $\mathbf{x}_1(0)$ which is used to integrate the (forward) equation (**??**) across $[0,T]$. This defines $\mathbf{x}_1(T)$ and therefore $\boldsymbol{\nu}_1(T)$ which 'initiates' the dual equation (47) so that this can be integrated backward in time to $t=0$. The 'final' dual state $\boldsymbol{\nu}_1(0)$ along with $\mathbf{x}_1(0)$ is then used to specify $\delta\mathcal{L}/\delta\mathbf{x}(0)$ so that the initial condition can be moved in the direction which increases $\mathcal{L}$ (λ is set by insuring that the new initial condition $\mathbf{x}_2(0)$ still has the initial energy E_0: see step 4 above). The *minimal seed* is then given by

$$\mathbf{x}_{ms} := \underset{\mathbf{x}(0):\mathbf{x}(t\to\infty)\neq\mathbf{0}}{\arg\min} E(\mathbf{x}(0)) \tag{50}$$

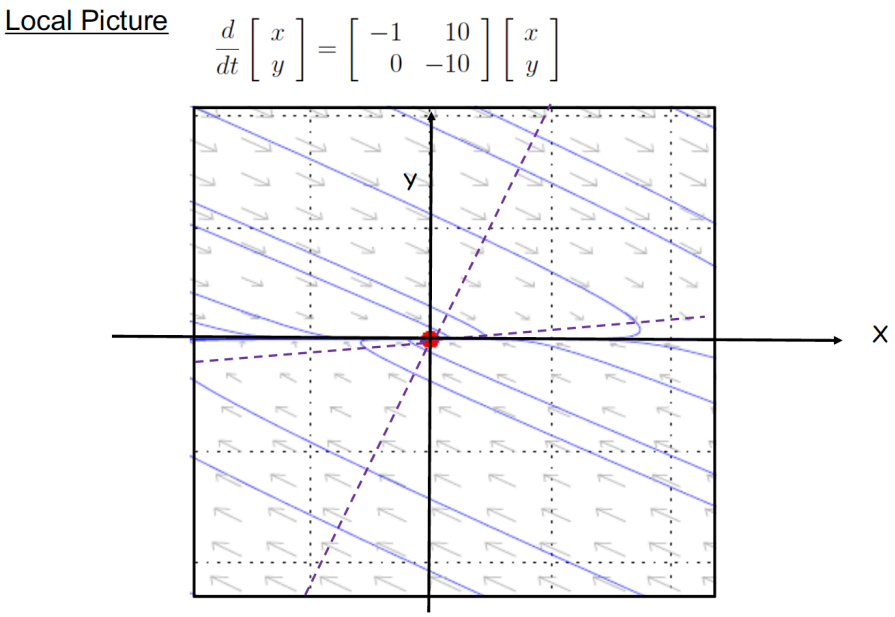

Figure 5: Local picture of the dynamics around $\mathbf{x} = \mathbf{0}$ for the 2D model (44) revealed by linear transient growth analysis. The dashed lines indicate where growth starts (the trajectory begins to move away from the origin) and finishes (where the trajectory turns back towards the origin). Notice that the environment is 2-fold rotationally symmetric about the origin.

with the corresponding least energy needed to escape the basin being $E(\mathbf{x}_{ms})$.

Figure 5 shows the behaviour of trajectories in the local environment of $\mathbf{x} = \mathbf{0}$. Linear transient growth analysis captures all the key features, for example, initial conditions where energy growth starts and finishes (the dashed lines). The picture is only local, however, as is highlighted by figure 6 which shows a more global picture of the phase plane. The minimal seed analysis is a two-stage process. The first stage - figure 7 - considers the maximum growth $G(T, E_0)$ over a time window T for initial conditions which have a fixed energy E_0: in 2D, this is just a circle of initial conditions of radius $\sqrt{E_0}$ centred on $\mathbf{x} = \mathbf{0}$. The second stage is to then increase E_0 until G jumps in magnitude: see figure 8. Formally, using the definition (41),

$$G(\infty, E_0) = \begin{cases} E_t & E_0 > E_c \\ E_e & E_0 = E_c \\ 0 & E_0 < E_c \end{cases} \tag{51}$$

where E_t is the energy of the turbulent attractor $\mathbf{x} \approx (14, 1.4)$ and E_e is the energy of the saddle point $\mathbf{x} = (10, 1)$. Practically, T is always finite and the discontinuities are smoothed over where the smoothing is reduced by making T larger; see figure 10. The critical E_0 has one initial condition - the minimal seed $\mathbf{x}_{ms} = (0, 1)$ - outside the basin of attraction of the laminar state: see figure 9.

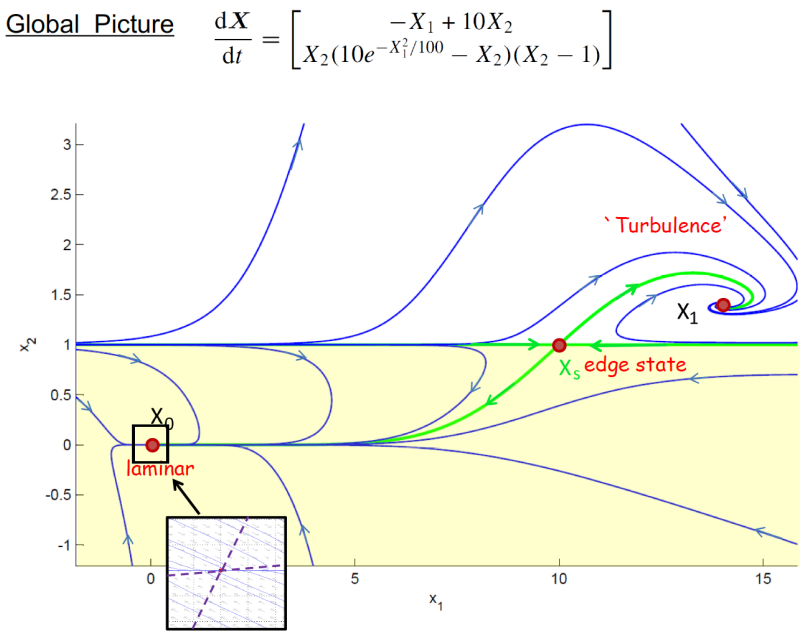

Figure 6: Global picture of the dynamics in the 2D model (44).

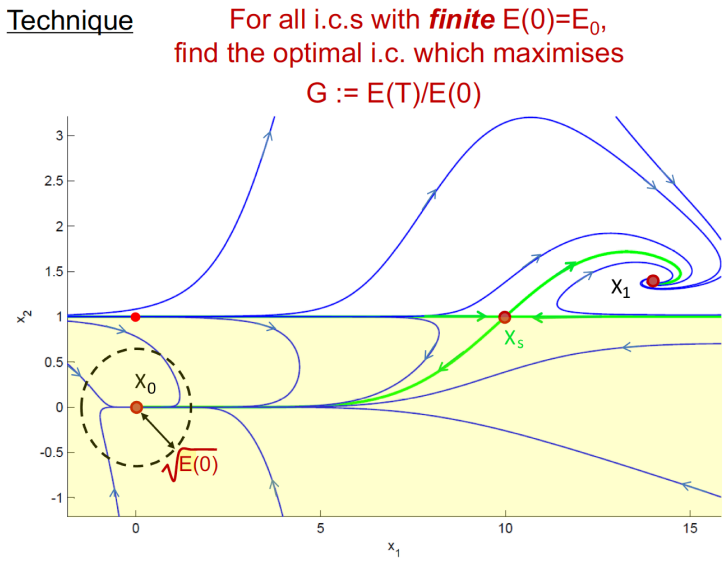

Figure 7: The constant-E_0 set of initial condition competitors for maximizing the energy growth at time T in the 2D model (44).

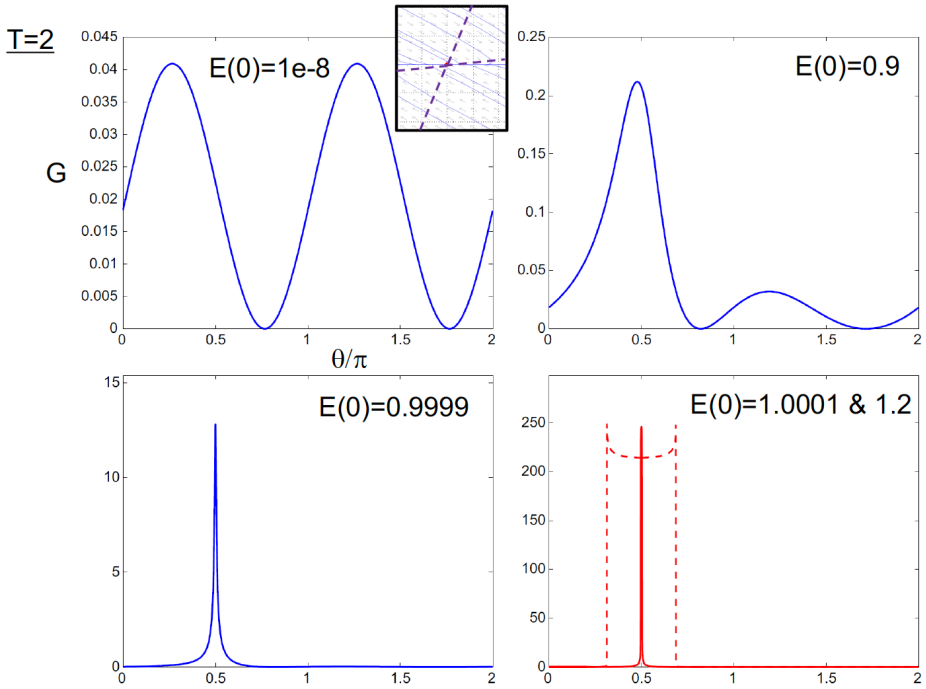

Figure 8: The result of calculating G as a function of θ/π where the initial condition is $\mathbf{x}(0) = \sqrt{E_0}(\cos\theta, \sin\theta)$ for various E_0. $E_0 = 10^{-8}$ reproduces the linear result which is symmetric under the transformation $\theta \to \theta + \pi$ and notice the sudden jump in G when E_0 crosses 1.

Technique II. Then increase E_0 until G shows a rapid change in value

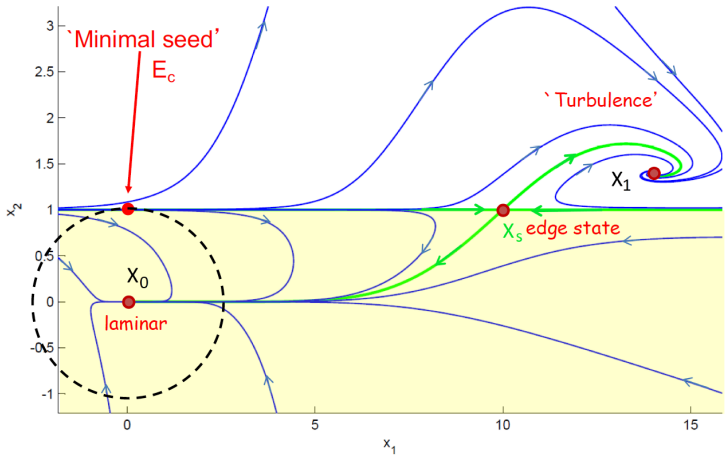

Figure 9: The minimal seed - here simply $\mathbf{x} = (0, 1)$ is the initial condition which first leaves the basin of attraction of $\mathbf{x} = \mathbf{0}$.

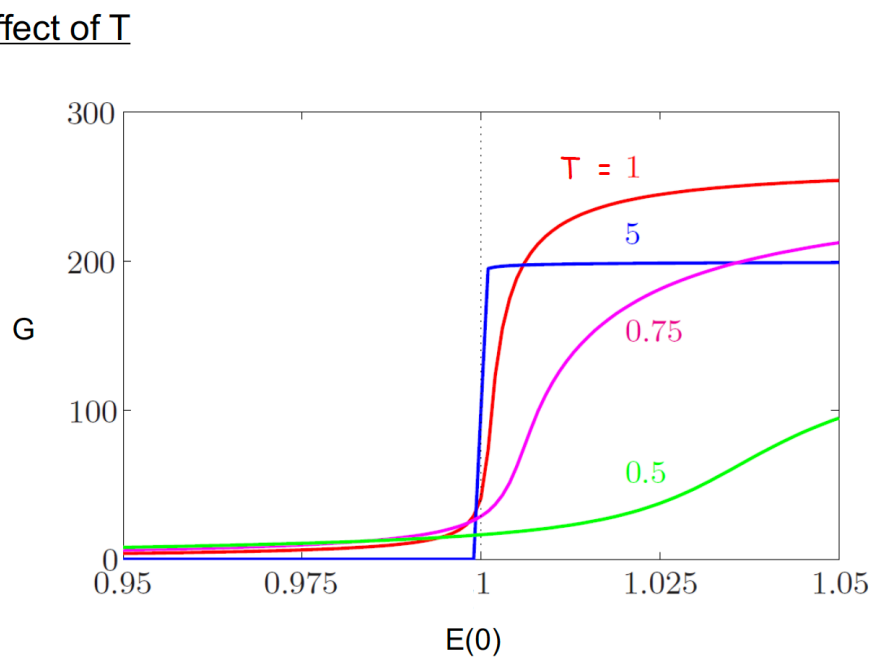

Figure 10: $G(T, E_0)$ versus E_0 for a variety of T for the 2D model (44): the larger T the clearer the value of $E(\mathbf{x}_{ms})$, the value of E_0 for the minimal seed, becomes.

We now show that this also works in the Navier-Stokes setting by studying flow in a pipe. Taking T as the time at which the maximum *linear* growth occurs ($0.0122Re\,D/U$ where D is the diameter and U is the bulk velocity), the optimal which emerges as a function of E_0 is shown in figure 11. For small E_0, a recognizably nonlinear version of the 2D linear optimal perturbation (LOP) is found (e.g. it stays 2D). This consists of streamwise rolls (see top left cross section in figure 12) which subsequently drives a pair of fast and slow streaks via the lift-up mechanism (b' and c' cross-sections in figure 12). Beyond a certain E_0, a new optimal is selected which is 3D and localized in both the radius and azimuth - see figure 12 below (it is also localized in the axial direction if the pipe domain is long enough: see figure 15). This so-called NLOP - nonlinear optimal perturbation - concatenates three well-known linear growth mechanisms which operate over different timescales whereby producing more growth (see right diagram in figure 11). A simple ODE model coupling two subspaces which exhibit transient growth albeit over different timescales can reproduce this effect very simply: see figure 13.

In pipe flow, this NLOP stays the optimal until a critical initial energy E_c is reached which means it smoothly connects to the minimal seed defined at $E_0 = E_c$. The significance of E_c is that the streaks produced by the NLOP become unstable and this instability leads to turbulence: see figure 14. In fact, because running the

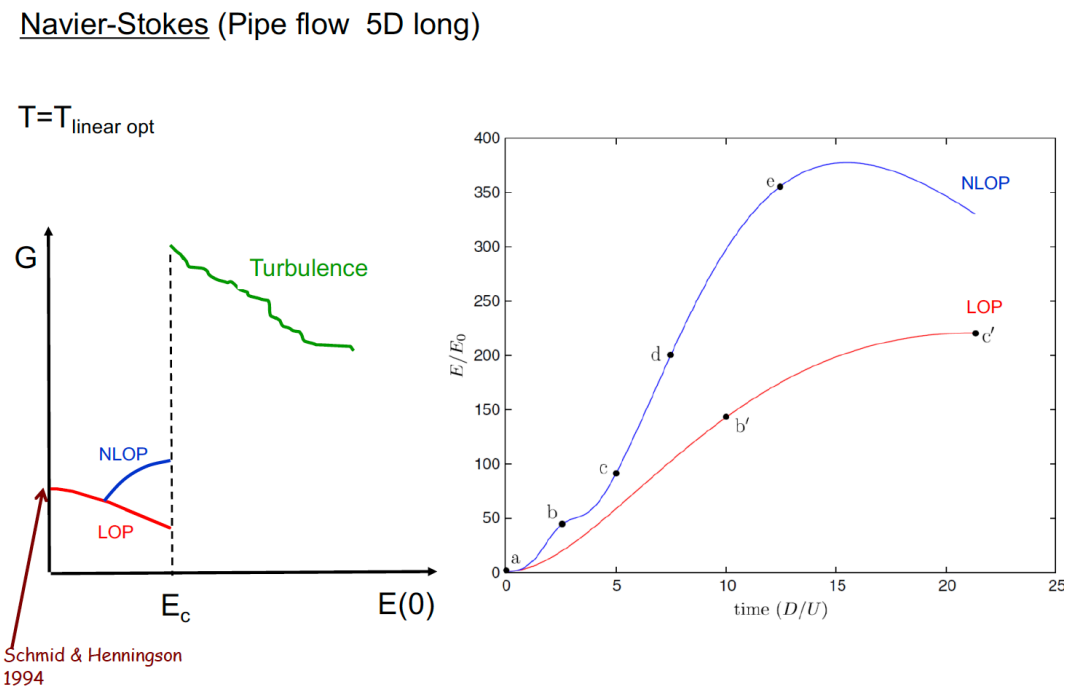

Figure 11: **Left**: A graph of growth G versus E_0 for a pipe 5 diameters long at $Re = 2400$ (the $E_0 \to 0$ LOP limit is given by [18]). **Right**: The evolution of the NLOP shows the concatenation of three linear processes: the Orr mechanism, oblique waves and the lift-up mechanism which together produce more growth than the LOP [14].

optimization procedure for $E_0 > E_c$ leads to turbulent trajectories and so convergence is then not possible due to the extreme sensitivity of the final energy to the initial conditions, the green curve shown schematically on the left of figure 11 is an average of G values found by the computations. However, practically this lack of convergence is easily diagnosed (turbulent endstates are reached) and can be used to identify E_c where convergence first *appears* (no turbulent endstates) as E_0 is *reduced*. The minimal seed as calculated in a long pipe 25 diameters long is shown in figure 15 confirming that it localizes in the axial direction too [15, 7]. NLOP calculations have also been performed in boundary layer flow [2], plane Couette flow [10, 16] and plane Poiseuille flow [4]: see the review [7].

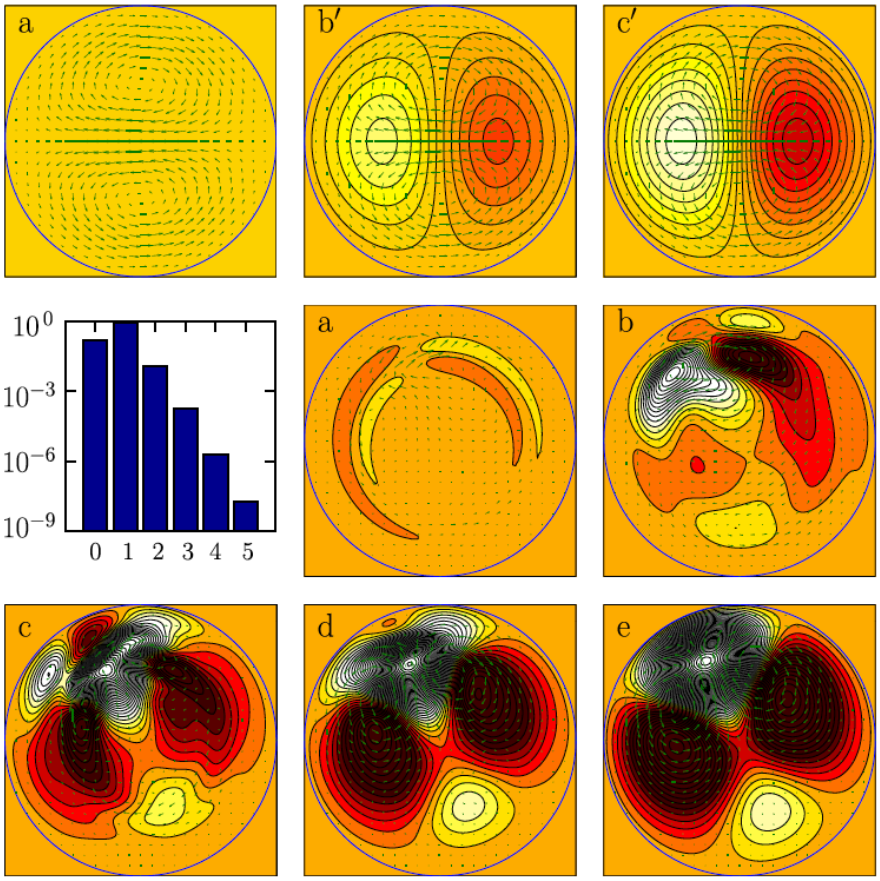

Figure 12: **Top row**: the linear optimal. **The rest**: the nonlinear optimal (the letters correspond to those indicating specific times in figure 11 (from [13]). The bar chart shows the ratio of energy in each streamwise Fourier mode of the NLOP to emphasize its nonlinearity (a linear optimal is monochromatic in axial wavenumber).

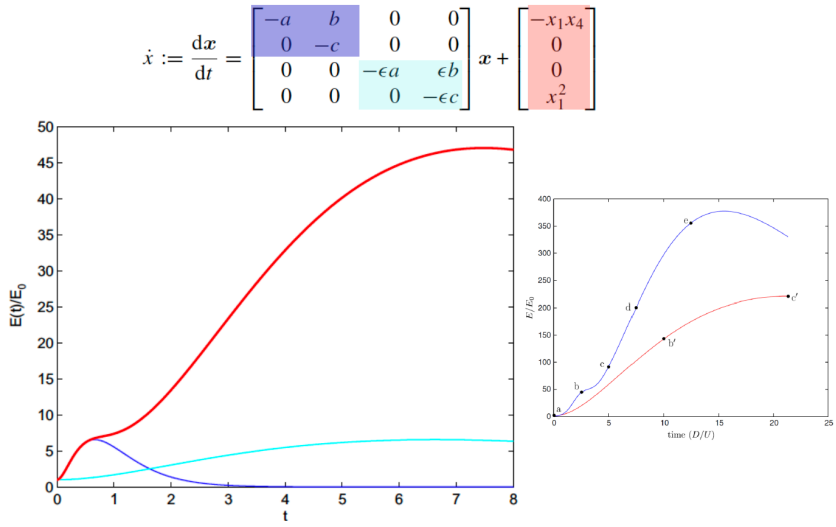

Figure 13: A simple model to explain the 'shoulder' in growth curve of figure 11. The blue curve and cyan curve indicate the linear transient growth possible for each of the two subspaces whereas the red curve is the nonlinear optimal produced when the coupling term is added. In this latter situation the transient growth in the blue subspace bootstraps the growth in the cyan subspace to produce much greater growth overall. Specifc parameters choices are $(a, b, c, d) = (1, 10, 2, 0, 1)$ from [8].

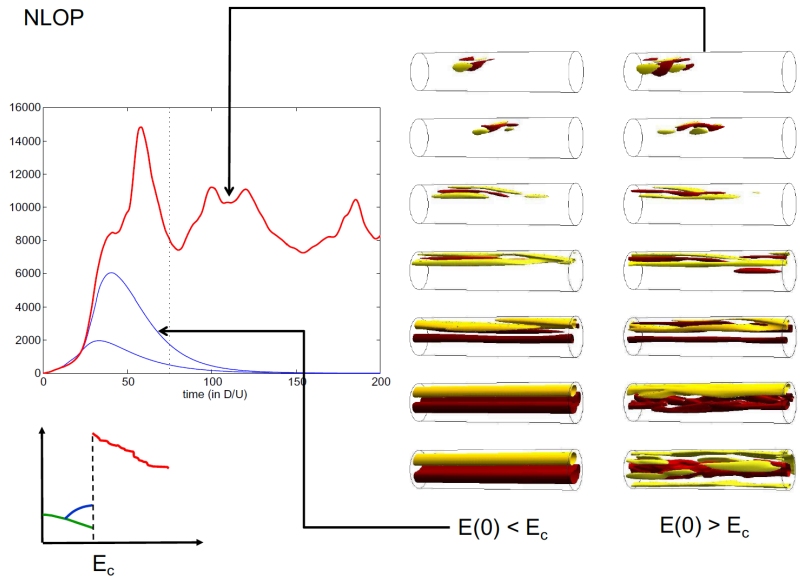

Figure 14: For $E_0 \lesssim E_c := E_0(\mathbf{x}_{ms})$, the optimal looks very similar to the minimal seed but in the ensuing evolution, the streaks do not break down (see **left** column of snapshots) whereas for $E_0 \gtrsim E_c := E_0(\mathbf{x}_{ms})$, the streaks do break down and turbulence is triggered (in fact, $\mathbf{x}(0)$ used to generate the **right** column of snapshots is a rescaled minimal seed).

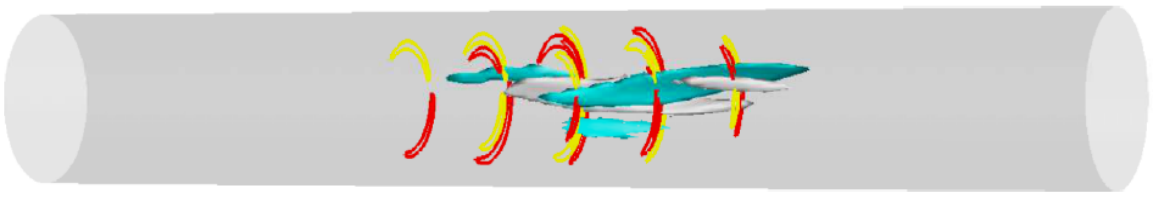

Figure 15: A 7-diameter section of the minimal seed from a 25-diameter pipe calculation with $Re = 2400$, radial, azimuthal and axial resolutions of $64 \times 48 \times 256$ and $T = 29.35$ (in time units of diameter/bulk speed), the optimal growth time for linear transient growth. Yellow & red contours indicate streaks and the white & green surfaces axial vorticity (from [15]).

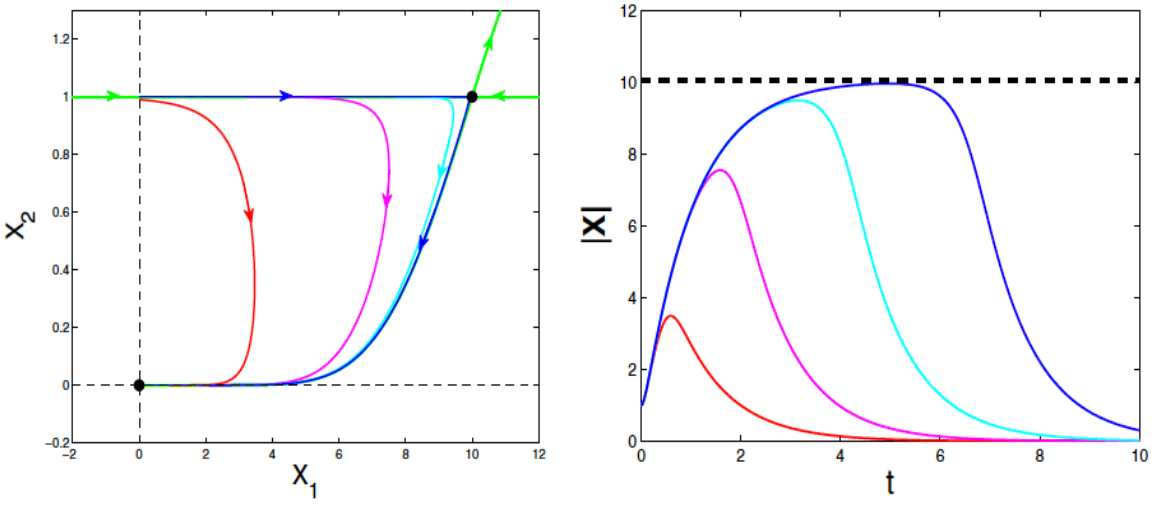

Figure 16: This plot illustrates that starting closer and closer to the stable manifold of a saddle point will give more and more of a plateau in the energy (actually the amplitude is plotted here). The plateau is where the dynamics hesitate in the neighbourhood of the saddle point. Calculations are performed for the 2D model 44 [12].

1.5 Probing Phase Space

The minimal seed procedure has been described above as a technique to find the least amplitude disturbances which put a system into a new basin of attraction i.e. to study transition between (at least) two attractors (for multiple attractors see [9]). The procedure, however, can be used to probe phase space more generally. In the below, we briefly discuss two different uses: searching for a) nearby saddle points and b) alternate transition scenarios not mediated by the edge state.

To illustrate a) we go back (again) to our 2D model (44). One can imagine a ball of radius $\sqrt{E_0}$ gradually expanding around the base state and the optimization algorithm latching on to any initial condition which approaches the stable manifold of a nearby saddle. Figure 16 shows what happens as the initial condition $(0, x_2)$ approaches the stable manifold of the edge state at $(10, 1)$. The figure on the right in 16 shows that the amplitude approaches and increasingly plateaus at $\sqrt{101}$ (the amplitude of the edge state) as $x_2 \to 1$.

In the Navier-Stokes equations, there is particular interest in seeing if solutions exist in certain parts of parameter space (particularly the gap between the energy stability point and the currently known emergence of alternative solutions, e.g. in plane Couette flow, this gap is $20.7 < Re < 127.7$ [12]), and finding localized solutions. We focus on the latter here[2] and speculate that a typical situation would be like that sketched in figure 17 where the stable manifold of a localised state should be closer to the base state than the stable manifold of a global solution which has larger amplitude and should be more distant. This at least seems the case for computations performed in wide-domain plane Couette flow [12] where it is known both global and localised solutions exist at $Re = 180$ [19]: see figure 18.

The calculations were performed in a wide domain $4\pi \times 2 \times 16\pi$ and initiated with random initial conditions (energy scattered in the lowest modes) normalized so that the total kinetic energy was E_0. If E_0 is too small, only the immediate neighborhood of the constant shear solution is explored with a nonlinear version of the 2D linear optimal, a global set of streamwise rolls, emerging as the optimal. If E_0 is too large, the optimal perturbation leads to another global state resembling multiple copies of Nagata's solution (see the top cross-section in figure 18). At intermediary E_0, the optimal perturbation is more spanwise localized and stays spanwise localized as it evolves into a state suggestive of a snake solution. Taking a snapshot from the energy growth plateau (see the top right diagram in figure 19) and plugging this into a Newton-Raphson solver gives the snake solution (lower cross-section in figure 18 and lower right image in figure 19).

[2]For the former see [12].

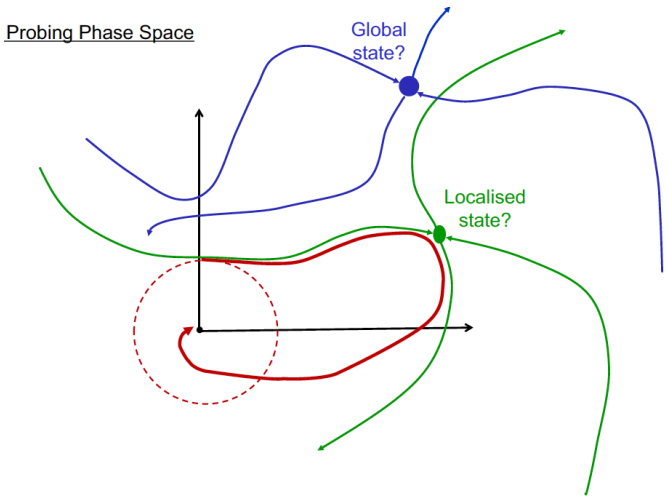

Figure 17: Phase space indicating that localized solutions should be closer (in an energy norm) to the base state than a global solution in an extended domain and hence found first as E_0 is increased from 0.

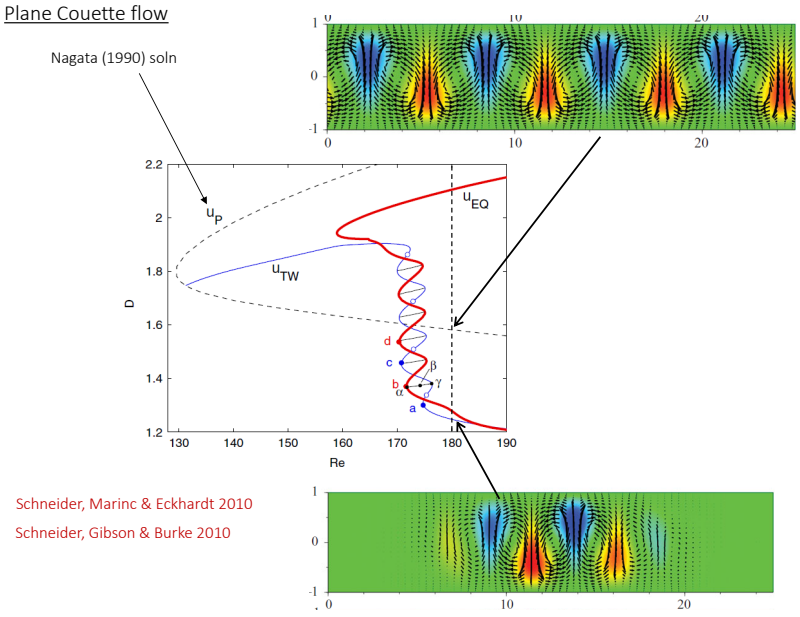

Figure 18: In plane Couette flow, the constant shear base state is provably a global attractor for $Re < 20.7$ [6]. However global states only start to appear beyond $Re = 127.7$ [11, 20] in saddle node bifurcations. Beyond this point, at about 175, localized solutions also appear [19]. So certainly at $Re = 180$, both global and localized states co-exist with the base flow.

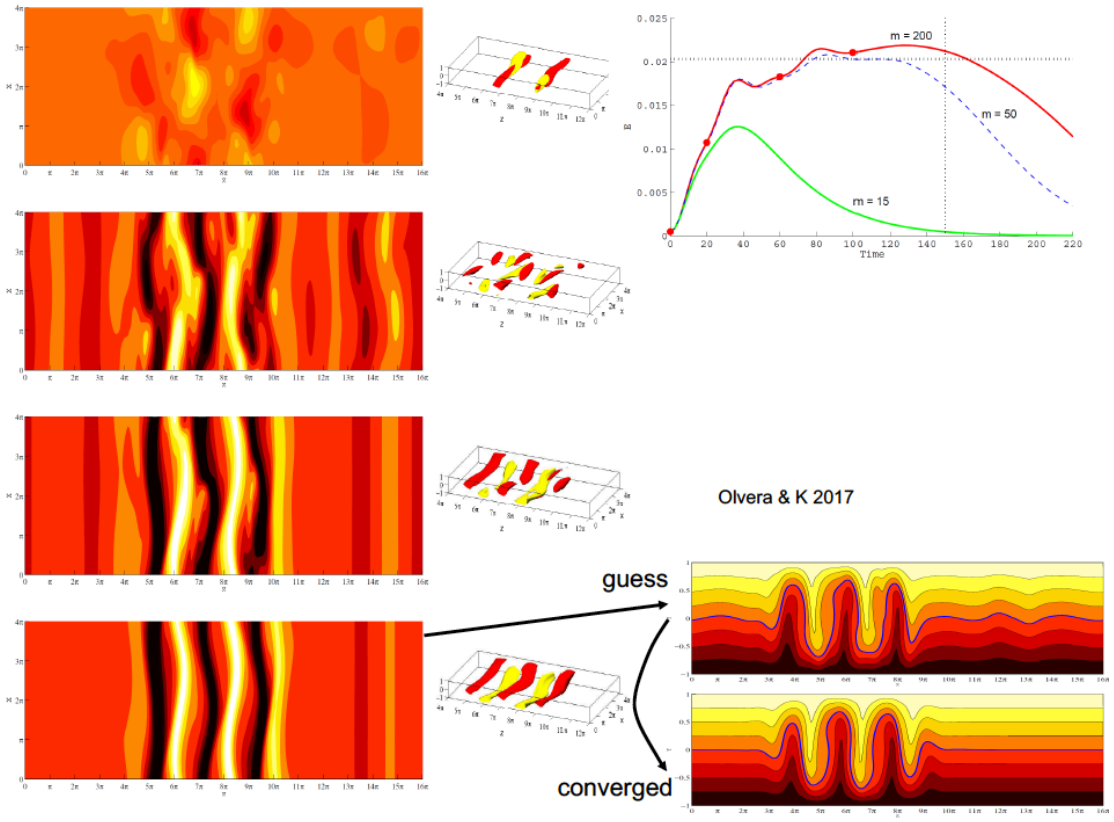

Figure 19: A nonlinear energy optimal calculation which shows 'plateauing' which indicates that an initial condition has been found near the stable manifold of a nearby saddle (here a localized state). A typical velocity snapshot is taken from the plateau and converged as the snake equilibrium of [19] from [12].

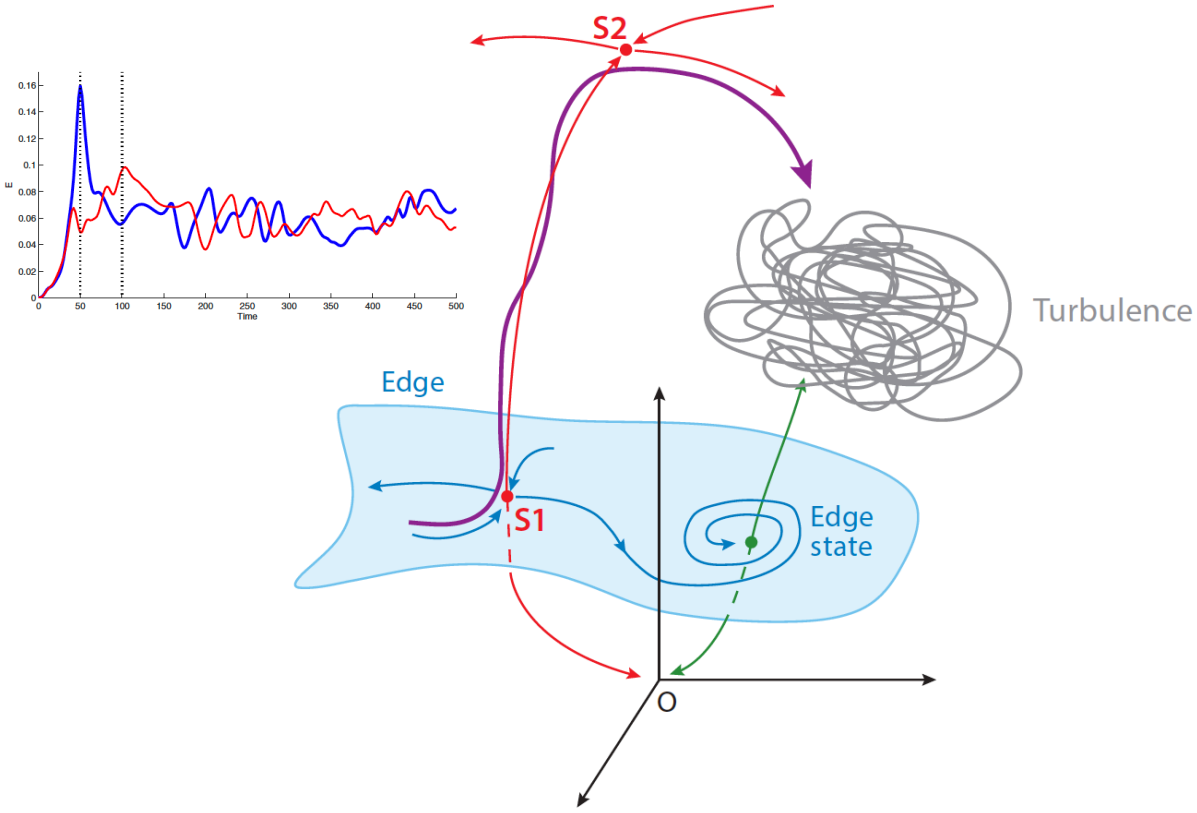

Figure 20: Nonlinear optimization can be used to find different transition scenarios. The schematic shows how a bursting transition can be found at higher disturbance energies than the minimal seed (which goes through the edge state). The inset shows the energy as a function of time for the two different scenarios: blue is the bursting situation and red is the (generic) edge state-mediated transition (see [12]).

We now show an example where an alternative transition scenario can be revealed - application b) - by optimising energy growth over different time scales. Figure 20 shows two evolutions obtained by optimising using $T = 50$ (blue line) and $T = 100$ (red line) for very weakly stratified plane Couette flow at $Re = 400$ and Richardson number $Ri_b = 1.0 \times 10^{-6}$ in a box of size $2\pi \times 2 \times \pi$ [12]. The longer time computation picks up the generic transition scenario mediated by the edge state whereas the shorter time reveals a 'bursting' transition where the energy reaches a much larger level during the transition than that achieved in the turbulent end state. A plausible rationalisation of what is happening is shown schematically in figure 20.

1.6 Summary 3

(*i*) Linear operators in shear flows are generically non-normal and therefore have non-orthogonal eigenvectors. This typically gives rise to transient growth for certain initial conditions.

(*ii*) The standard matrix-free approach to quantifying this can be easily extended to treat finite-amplitude disturbances.

(*iii*) This nonlinear nonmodal analysis can be coupled to a outer search in initial energy E_0 to identify where the maximal energy growth undergoes a sudden change in magnitude. The optimal initial condition at this point is the *minimal seed* - the disturbance of least amplitude which does not asymptote to the base state for large times.

(*iv*) The process of maximising energy growth over initial conditions of a given finite energy can also be used to find 'nearby' saddles in phase space as well as finding different routes of transition.

(*v*) Nonlinear optimization using the full Navier-Stokes equations as constraints is very flexible and so many novel applications are possible.

References

[1] C. D. Cantwell, D. Barkley, and H. M. Blackburn, *Transient growth analysis of flow through a sudden expansion in a circular pipe*, Physics of Fluids, 22 (2010), p. 034101.

[2] S. Cherubini, P. DePalma, J.-C. Robinet, and A. Bottaro, *Rapid path to transition via nonlinear localized optiml perturbations in a boundary layer*, Phys. Rev. E, 82 (2010), p. 066302.

[3] P. Corbett and A. Bottaro, *Optimal perturbations for boundary layers subject to stream-wise pressure gradient*, Physics of Fluids, 12 (2000), pp. 120–130.

[4] M. Farano, S. Cherubini, J.-C. Robinet, and P. De Palma, *Hairpin-like optimal perturbations in plane Poiseuille flow*, J. Fluid Mech., 775 (2016), p. R2.

[5] A. Guégan, P. J. Schmid, and P. Huerre, *Optimal energy growth and optimal control in swept Hiemenz flow*, Journal of Fluid Mechanics, 566 (2006), pp. 11–45.

[6] D. D. Joseph, *Nonlinear stability of the Boussinesq equations by the method of energy*, Arch. Rat. Mech. Anal., 22 (1966), pp. 163–184.

[7] R. R. Kerswell, *Nonlinear nonmodal stability theory*, Ann. Rev. Fluid Mech., 50 (2018), pp. 319–345.

[8] R. R. Kerswell, C. C. T. Pringle, and A. P. Willis, *An optimization approach for analysing nonlinear stability with transition to turbulence as an exemplar*, Rep. Prog. Phys., 77 (2014), p. 085901.

[9] D. Lecoanet and R. R. Kerswell, *Connection between nonlinear energy optimization and instantons*, Phys. Rev. E, 97 (2018), p. 012212.

[10] A. Monokrousos, A. Bottaro, L. Brandt, A. Di Vita, and D. S. Henningson, *Nonequilibrium thermodynamics and the optimal path to turbulence in shear flows*, Phys. Rev. Lett., 106 (2011), p. 134502.

[11] M. Nagata, *Three-dimensional finite-amplitude solutions in plane Couette flow: bifurcation from infinity*, J. Fluid Mech., 217 (1990), pp. 519–527.

[12] D. Olvera and R. R. Kerswell, *Optimizing energy growth as a tool for finding exact coherent structure*, Phys. Rev. Fluids, 2 (2017), p. 083902.

[13] C. C. T. Pringle and R. R. Kerswell, *Using nonlinear transient growth to construct the minimal seed for shear flow turbulence*, Phys. Rev. Lett., 105 (2010), p. 154502.

[14] C. C. T. Pringle, A. P. Willis, and R. R. Kerswell, *Minimal seeds for shear flow turbulence: using nonlinear transient growth to touch the edge of chaos*, Journal of Fluid Mechanics, 702 (2012), pp. 415–443.

[15] ——, *Fully localised nonlinear energy growth optimals in pipe flow*, Phys. Fluids, 27 (2015), p. 064102.

[16] S. M. E. Rabin, C. P. Caulfield, and R. R. Kerswell, *Variational identification of minimal seeds to trigger transition in plane Couette flow*, J. Fluid Mech., 712 (2012), pp. 244–272.

[17] S. C. Reddy and D. S. Henningson, *Energy growth in viscous channel flows*, Journal of Fluid Mechanics, 252 (1993), pp. 209–238.

[18] P. J. Schmid and D. S. Henningson, *Optimal energy density growth in Hagen-Poiseuille flow*, Journal of Fluid Mechanics, 277 (1994), pp. 197–225.

[19] T. M. Schneider, J. F. Gibson, and J. Burke, *Snakes and ladders: localized solutions of plane Couette flow*, Phys. Rev. Lett., 104 (2010), p. 104501.

[20] F. Waleffe, *Homotopy of exact coherent structures in plane shear flows*, Phys. Fluids, 15 (2003), pp. 1–18.